Analytical Model for Composite Transverse Strength based on Computational Micromechanics

Sagar P. Shah and Marianna Maiarù*

University of Massachusetts Lowell, Lowell, MA - 01854, USA.

*Corresponding Author

Abstract

The transverse strength of fiber-reinforced composites is a matrix-dominated property whose accurate prediction is crucial to designing and optimizing efficient, lightweight structures. State-of-the-art analytical models for composite strength predictions do not account for fiber distribution, orientation, and curing-induced residual stress that greatly influence damage initiation and failure propagation at the microscale. This work presents a novel methodology to develop an analytical solution for transverse composite strength based on computational micromechanics that enables the modeling of stress concentration due to Representative Volume Elements (RVE) morphology and residual stress. Finite element simulations are used to model statistical samples of composite microstructures, generate stress-strain curves, and correlate statistical descriptors of the microscale to stress concentration factors to predict transverse strength as a function of fiber volume fraction. Tensile tests of thin plies validated this approach for carbon- and glass-reinforced composites showing promise to obtain a generalized analytical model for transverse composite strength prediction.

Keywords – Transverse tensile strength, analytical modeling, computational micromechanics, damage mechanics

1 Introduction

Designing advanced composite parts for engineering and structural applications is extremely time-consuming as it often involves expensive and lengthy experimental campaigns or complex and time-intensive computational modeling [1]. It is paramount to expedite the composite design and certification process to meet their ever-increasing demand. Analytical models can be used as efficient predictive tools to estimate composite response from constituent material properties, especially in problems involving many design variables for optimization [2, 3], if their relative error with respect to experimental measurements is contained. State-of-the-art models employ either physics-based formulations or empirical relations to correlate the overall composite response to their constituent structures and properties. Analytical models provide significant advantage of simple implementation and computation over experiments and high-fidelity computational models for structural design and optimization [4].

The literature presents numerous analytical models that can estimate the elastic property of polymer matrix composites (PMCs) from their constituent properties. For instance, classical theories such as rule-of-mixture (ROM), modified rule-of-mixture (MROM) and enhanced models such as the continuous periodic fiber model (CPFM), the concentric cylindrical assembly (CCA), Mori-Tanaka (MT), and the Bridging Model (BM), have been widely employed to predict composite elastic response [3–14]. However, there are only a few micromechanical strength theories that can accurately predict the composite strength from its constituent properties [2, 6, 8, 15–17]. Huang et al. [6] developed the BM to estimate the stress field inside a single-fiber repeating unit cell (RUC) with square packing. They introduced a stress concentration factor (SCF) within the RUC to compute the in-situ matrix strength which was then used in conjunction with explicit micromechanical formulae to evaluate the transverse composite strength. Their model presented an average error of 40% when compared with transverse strengths of nine unidirectional (UD) composite laminates. Vignoli et al. [2] developed an elasticity-based model for transverse strength prediction. They established analytical solutions to estimate the stress distribution around a single-fiber in an infinite medium. Combining them with finite element (FE) approach, adjustments functions were defined to determine the stress distribution in a more realistic square-packed RUC of several fiber volume fractions. Finally, the transverse strengths were predicted based on the matrix cavitation model. Their predictions presented an average error between 25% and 40% when compared to experimental data as well as other simplified analytical models. These models, among others, were developed based on a simplified mathematical representation of a composite microstructure, or a single-fiber square RUC [2, 3, 8, 18, 19]. Thus, they failed to account for inter-fiber interactions and the resulting stress concentration distribution that is observed in a multi-fiber representative volume element (RVE). Furthermore, the models did not consider the effect of process-induced in-situ matrix property variation and residual stress generation on the transverse composite strength. It is well known that random fiber packing and residual stress generation not only influence the failure initiation in composite microstructures, but also drive failure propagation under continued loading [4,20–27]. Existing analytical models ignore these effects and

therefore present a lower correlation with transverse composite strength tests. Computational micromechanics-based simulations can fill these knowledge gaps and address the fundamental challenges associated with analytical models in order to enhance their prediction accuracy.

Over the past few decades, advances in high-performance computing, finite element methods (FEM) and novel physics-based constitutive modeling have facilitated the design and development of PMCs through computational methods [28–30]. Computational micromechanics is an emerging field that leverages these advances to model and analyze RVEs of composite microstructures by subjecting them to various thermo-mechanical boundary conditions [30–50]. Such analysis can provide valuable insights into the fundamental mechanisms that influence the composite response at the constituent-level, thereby overcoming the limitations associated with experimental quantification [30]. By explicitly modeling the constituent fibers and matrix, phenomena such as stress concentration due to random fiber packing and fiber-to-fiber proximity, that induce matrix cracking under transverse tensile loading conditions and significantly influence the transverse composite strength, can be studied with relative ease and efficiency. FE-based process modeling simulations, which are informed by accurate and comprehensive material characterization and employ phenomenological and constitutive relations, can facilitate the quantification of residual stress build-up within composite RVEs during manufacturing. Virtually curing and loading RVEs in transverse tension can provide insight on the impact of process-induced residual stresses and random fiber distribution on transverse composite strength. The knowledge gained from computational micromechanical analysis of composite RVEs can be leveraged to establish a processing-microstructure-property relationship and address the aforementioned fundamental challenges to develop an accurate computational micromechanics-based analytical model for transverse strength.

The objective of this work is to present a novel methodology to develop a computational micromechanics-based analytical model for transverse tensile strength prediction. In this study, FE-based, computational micromechanical models are generated to analyze a wide array of composite microstructures for their transverse composite strengths. It is hypothesized that random fiber packing and the resulting stress concentration induce failure within the microstructures, which affects their transverse strength. Based on this hypothesis, a generalized expression for transverse strength is discussed. Critical parameters that influence the transverse composite strength are highlighted. The concept of a stress concentration factor induced by a single-fiber RUC is presented. The influence of relative fiber arrangement (distance between fiber centers and their orientation) on the SCF is then quantified through FE simulations of two-fiber model. Leveraging the insights from the two-fiber SCF study, a statistical approach to quantify the SCF in multi-fiber microstructures is presented. Finally, a material system-specific analytical model for transverse composite strength is developed. It is shown that insights from computational models can inform the development of mathematical relations to correlate the microscale physical mechanisms such as stress concentration to composite failure and predict transverse strength of multi-fiber composite microstructures.

This manuscript is organized as follows: the computational micromechanical modeling approach is detailed

in Section 2, the development of the analytical model is described in Section 3 and the concluding remarks are discussed in Section 4.

2 Computational Micromechanics

Computational micromechanics requires efficient yet sufficiently large models to capture the physical mechanisms that induce failure. In this study, converged RVEs including 50 fibers were analyzed based on the results of a statistical size-effect study performed previously by Shah et al. [32]. The modeling details and virtual manufacturing and testing procedures are discussed in the following sections.

2.1 Modeling of composite microstructures

In this study, two sets of RVEs comprising a random dispersion of IM7 carbon (fiber diameter, $d_{\mathrm{f}} = 6\ \mu$m) and E-glass fibers ($d_{\mathrm{f}} = 14\ \mu$m) in an epoxy matrix, respectively were generated using a random RVE generator developed by Stapleton et al. [51]. A commercial epoxy system, EPIKOTE$^{\mathrm{TM}}$ Resin MGS RIMR 135 with EPIKURE$^{\mathrm{TM}}$ Curing Agent MGS RIMH 1366 (henceforth referred to as RIM R135-H1366), was chosen as the matrix material due to its comprehensive thermo-mechanical material property dataset reported in [31]. Several composite microstructures, corresponding to various fiber volume fractions ($0.25 \leq v_{\mathrm{f}} \leq 0.75$) were considered, as illustrated in Figure 1 and summarized in Table 1. To improve the prediction accuracy and to account for statistical variations due to random fiber architecture, five distinct replicates with random fiber distribution were analyzed for each value of v_{f} . Perfect bonding was assumed between the fibers and the matrix. Due to their nature, the constituent IM7 carbon fibers were modeled as transversely-isotropic while the E-glass fibers were modeled as isotropic solids. The thermo-mechanical properties for both constituent fiber materials are summarized in Table 2. The matrix material was modeled as isotropic. The evolution of the matrix thermo-mechanical properties with the degree of cure ϕ and the processing temperature T during virtual manufacturing was defined by experimentally-determined material-specific models described in [31]. These properties, for a fully cured matrix ($\phi = 1$), are also listed in Table 2. Failure was admissible only in the matrix material when the maximum principal stresses exceeded its critical strength.

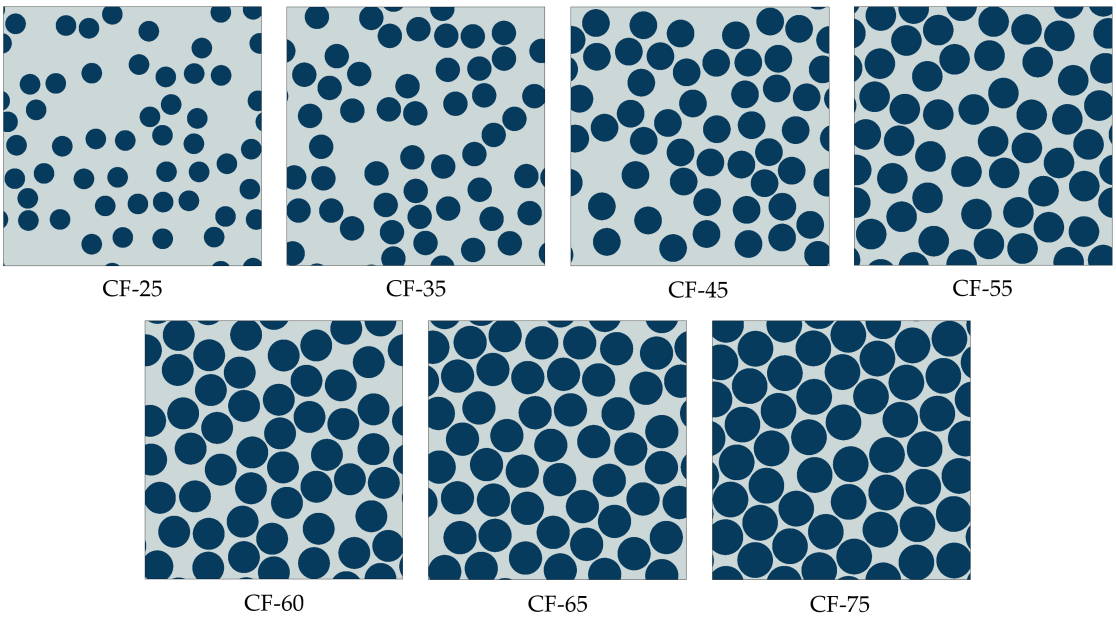

(a) IM7 carbon fibers RVEs

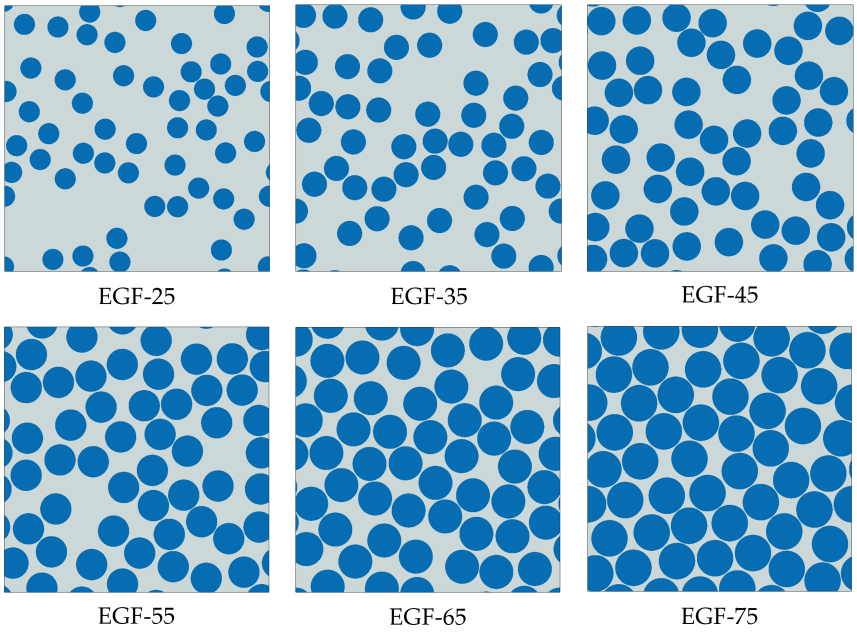

(b) E-glass fiber RVEs

Figure 1: Various realizations of (a) IM7 carbon fibers (CF) and (b) E-glass fibers (EGF) embedded in RIM R135-H1366 epoxy matrix with varying fiber volume fractions $25\% \leq v_{\mathrm{f}} \leq 75\%$.

Table 1: Details of composite microstructures analyzed in this study.

Material	**RVE ID**	**RVE length** (μm)	**No. of fibers**	$\boldsymbol{v_f}$ (-)
IM7 carbon fiber ($d_f = 6$ μm)	CF-25	75.2	50	0.25
	CF-35	63.5	50	0.35
	CF-45	56.0	50	0.45
	CF-55	50.7	50	0.55
	CF-60	48.5	50	0.60
	CF-65	46.6	50	0.65
	CF-75	43.4	50	0.75
E-glass fiber ($d_f = 14$ μm)	EGF-25	175.5	50	0.25
	EGF-35	148.3	50	0.35
	EGF-45	130.8	50	0.45
	EGF-55	118.3	50	0.55
	EGF-65	108.8	50	0.65
	EGF-75	101.3	50	0.75

Table 2: Thermo-mechanical properties of the constituent fibers and epoxy matrix.

Property	**Units**	**IM7 carbon**	**E-glass**	**RIM R135-H1366**
Density, ρ	[kg/m^3]	1780	2550	1200
Axial Modulus, E_{11}	[MPa]	276000	73000	2482
Transverse Modulus, $E_{22} = E_{33}$	[MPa]	19500	73000	2482
In-plane Poisson's ratio, $\nu_{12} = \nu_{13}$	[-]	0.28	0.22	0.37
Out-of-plane Poisson's ratio, ν_{23}	[-]	0.25	0.22	0.37
In-plane Shear Modulus, $G_{12} = G_{13}$	[MPa]	70000	30000	905.8
Out-of-plane Shear Modulus, G_{23}	[MPa]	7800	30000	905.8
Critical Tensile Strength, σ_{cr}	[MPa]	–	–	64.1
Mode I Fracture Energy, G_{IC}	[J/m^2]	–	–	0.001
Axial CTE, α_{11}	[K^{-1}]	-0.54$\times10^{-6}$	5$\times10^{-6}$	73.9$\times10^{-6}$
Transverse CTE, $\alpha_{22} = \alpha_{33}$	[K^{-1}]	10.08$\times10^{-6}$	5$\times10^{-6}$	73.9$\times10^{-6}$
Thermal Conductivity, k	[W/m-K]	5.4	1.2	0.245
Specific Heat, c_p	[J/kg-K]	879	800	1600

The virtual manufacturing and mechanical testing procedures were carried out with the commercial FE code Abaqus/STANDARD, supplemented with user-written UMATHT and UMAT subroutines, the implementations of which are detailed in [31, 32] and summarized in the following section. Each RVE was meshed with C3D8T elements (eight-node, brick elements with temperature degrees of freedom). Flat boundary conditions (FBCs) were chosen for both virtual manufacturing and mechanical testing, as illustrated in Figures 2a and 2b, respectively [32].

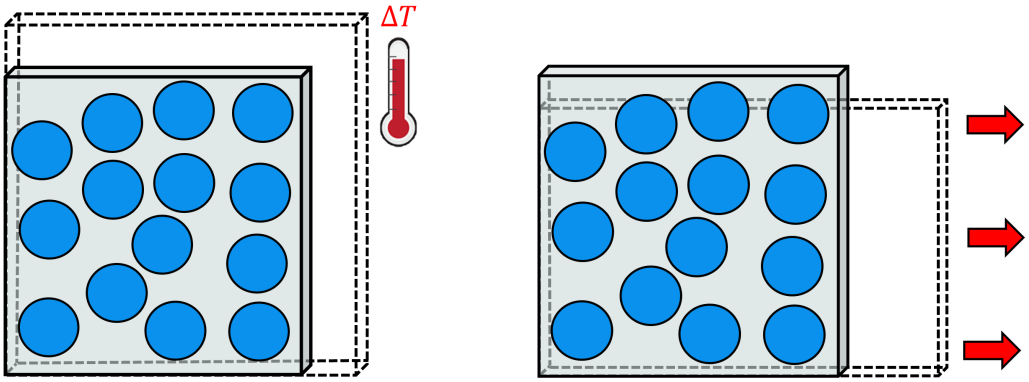

(a) Virtual manufacturing

(b) Virtual mechanical testing

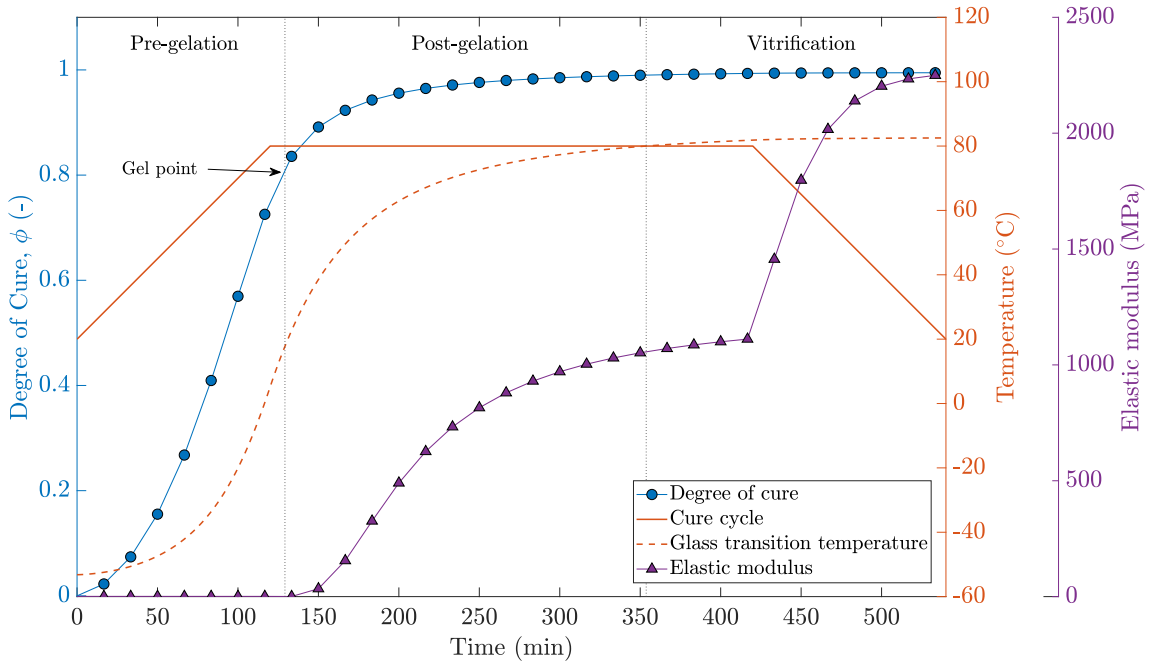

(c) Cure and thermo-mechanical property evolution for a prescribed cure cycle

Figure 2: Illustration of flat boundary conditions (FBCs) prescribed to the RVEs during: (a) virtual manufacturing and (b) virtual mechanical testing analyses; (c) evolution of the degree of cure ϕ, glass transition temperature T_g and the elastic modulus E for a prescribed cure cycle.

2.2 Virtual manufacturing

The virtual manufacturing analysis replicated the complete manufacturing of composites by accounting for (a) the kinetic progression of the cure which was quantified by ϕ and (b) the evolution of the in-situ thermo-mechanical matrix properties which led to residual stress generation. The progression of cure, for a prescribed temperature profile, was defined by the Kamal-Sourour kinetic model [52],

$$\frac{\mathrm{d}\phi}{\mathrm{d}t} = \left(K_1 + K_2\phi^m\right)(1-\phi)^n \tag{1a}$$

$$K_\mathrm{i} = A_\mathrm{i}\exp\left(\frac{\Delta E_\mathrm{i}}{RT^*}\right) \qquad \mathrm{i} = 1,2 \tag{1b}$$

where K_1 and K_2 are Arrhenius rate functions; $m = 0.4$ and $n = 1.5$ are dimensionless, real modeling parameters; $A_1 = 3.6 \times 10^9$ sec^{-1} and $A_2 = 0.01245$ sec^{-1} are pre-exponential factors; $\Delta E_1 = 85.3$ kJ/mol and $\Delta E_2 = 11.1$ kJ/mol are activation energies; T^* is the absolute temperature in degrees Kelvin; R is the universal gas constant. The kinetic constants were experimentally determined as reported in [31]. The kinetic model was solved simultaneously with the 3-dimensional Fourier heat transfer model in a coupled-temperature displacement analysis, carried out in Abaqus/STANDARD with user-subroutine UMATHT, to predict the progression of cure and the temperature distribution resulting from the exothermic heat of reaction during curing. The prescribed cure cycle and the computed degree of cure is presented in Figure 2c.

The evolution of the in-situ matrix properties and residual stress generation was modeled with UMAT user subroutine. For a given cure state, the instantaneous material properties were computed using experimentally-determined material-specific models reported in [31]. For instance, the variation of the in-situ matrix elastic modulus E with ϕ and T (see Figure 2c) was defined by

$$E = A_2(\phi) + \frac{A_1(\phi) - A_2(\phi)}{1 + \exp\left(\frac{\eta - \eta_0(\phi)}{\mathrm{d}\eta(\phi)}\right)} \tag{2}$$

where the dimensionless phenomenological parameters η, η_0, $\mathrm{d}\eta$, A_1 and A_2 were determined as a function of ϕ and T by the following expressions

$$\eta = 1 - \frac{T^*}{T^*_{\mathrm{r}}} \tag{3a}$$

$$\eta_0 = -0.860\phi + 0.955 \tag{3b}$$

$$\mathrm{d}\eta = 0.070\phi + 0.041 \tag{3c}$$

$$A_1(\phi) = -10^{-13}\exp(34.55\phi) \tag{3d}$$

$$A_2(\phi) = 1471.3\phi + 801.39 \tag{3e}$$

where T^*_{r} is the reference temperature in degrees Kelvin. Similarly, the evolution of the matrix glass transition temperature T^{ϕ}_{g} (see Figure 2c), post-gelation chemical shrinkage $\epsilon^{\phi}_{\mathrm{sh}}$ and post-gelation coefficient of thermal expansion $\alpha^{\phi}_{\mathrm{i}}$ were determined using the following equations

$$T^{\phi}_{\mathrm{g}} = T^0_{\mathrm{g}} + \frac{\lambda\phi}{1 - (1-\lambda)\phi}\left(T^1_{\mathrm{g}} - T^0_{\mathrm{g}}\right) \tag{4a}$$

$$\epsilon^{\phi}_{\mathrm{sh}} = \begin{cases} 0, & \phi \le \phi_{\mathrm{gel}} \\ \beta\left(\phi - \phi_{\mathrm{gel}}\right), & \phi > \phi_{\mathrm{gel}} \end{cases} \tag{4b}$$

$$\alpha^{\phi}_{\mathrm{i}} = \begin{cases} 7.93 \times 10^{-5}, & T \le T^{\phi}_{\mathrm{g}} \\ \left[a - b\left(\phi - \phi_{\mathrm{gel}}\right)\right] \times 10^{-5}, & T > T^{\phi}_{\mathrm{g}} \end{cases} \tag{4c}$$

where $T_g^0 = -53.2°C$ and $T_g^1 = 85.6°C$ are glass transition temperatures of uncured and fully cured matrix; $\beta = 0.111$ is the shrinkage coefficient; $\phi_{gel} = 0.78$ is the gel point (see Figure 2c); $\lambda = 0.2373$, $a = 21.21$ and $b = 18.25$ are dimensionless fitting parameters. An instantaneous linear-elastic constitutive model was then employed to model the residual stress generation in the material during curing

$$\sigma_i(t) = [C_{ij}(t)] \left[\epsilon_j^{total}(t) - \left(\epsilon_j^{th}(t) + \epsilon_j^{sh}(t)\right) \delta_j\right] \quad \text{where,} \begin{cases} \delta_j = 1 \text{ if j} = 1, 2, 3 \\ \delta_j = 0 \text{ if j} > 3 \end{cases} \tag{5}$$

where i and j are Voigt notation indices; $\epsilon_j^{total}(t)$, $\epsilon_j^{th}(t)$ and $\epsilon_j^{sh}(t)$ are the total, thermal and chemical shrinkage strains, respectively; $C_{ij}(t)$ is the stiffness matrix as a function of the time of cure; $\sigma_i(t)$ is the accumulated residual stress governed by the development of the in-situ matrix elastic modulus and the chemical and thermal strains experienced by the matrix. In this study, the curing matrix was prescribed a constant strength and fracture toughness as listed in Table 2.

As the matrix material, subjected to the temperature profile shown in Figure 2c, cured, its elastic modulus developed as illustrated in Figure 2c. This, combined with the matrix chemical shrinkage and thermal mismatch between the constituent fiber and matrix, resulted in self-equilibrating residual stress generation. The contour plot of the residual stresses (maximum principal), at the end of the cure, is shown for one representative IM7 carbon and E-glass fiber microstructure in Figures 3a and 3b, respectively. These RVEs, which consisted of a random dispersion of 50 fibers with a volume fraction of 0.6 and 0.55, respectively registered a maximum residual stress generation of 21.48 MPa and 24.58 MPa. The same microstructures reported a volume-averaged residual stress of 6.38 MPa and 7.49 MPa, respectively. These maximum and volume-averaged residual stress values differed considerably between RVEs owing to the different constituent fiber material properties, their unique fiber packing topology and the varying fiber volume fractions. Between the IM7 carbon fiber RVEs with $v_f = 0.6$, there was a maximum and volume-averaged end-of-cure residual stress of 20.93 ± 0.46 MPa and 6.406 ± 0.073 MPa, respectively. The E-glass fiber RVEs, with $v_f = 0.55$ reported a maximum and volume-averaged end-of-cure residual stress of 24.79 ± 1.1 MPa and 7.89 ± 0.44 MPa, respectively.

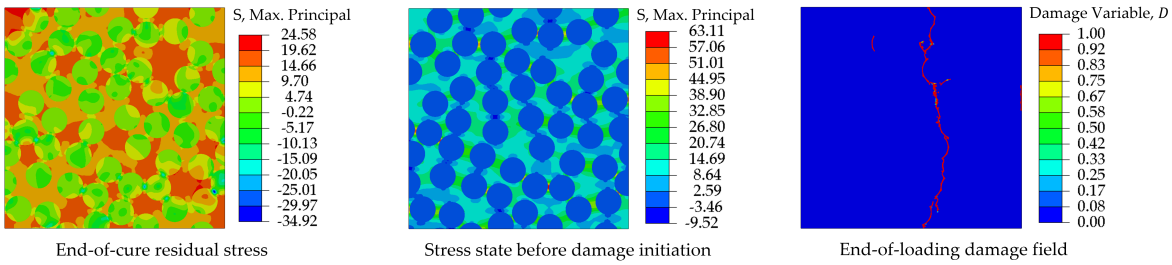

(a) IM7 carbon fiber RVE ($v_f = 0.60$)

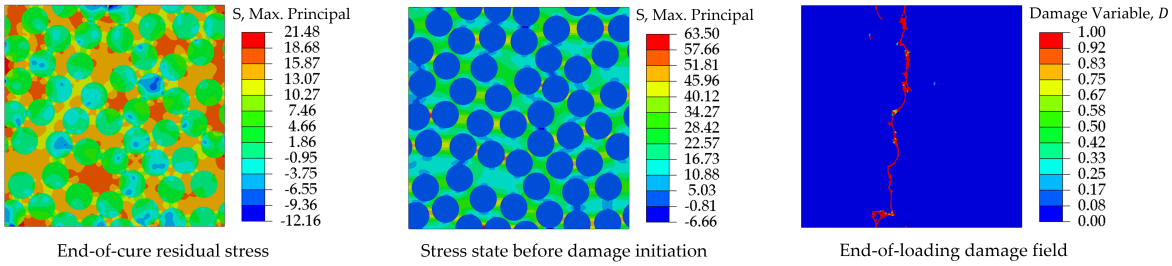

(b) E-glass fiber RVE ($v_f = 0.55$)

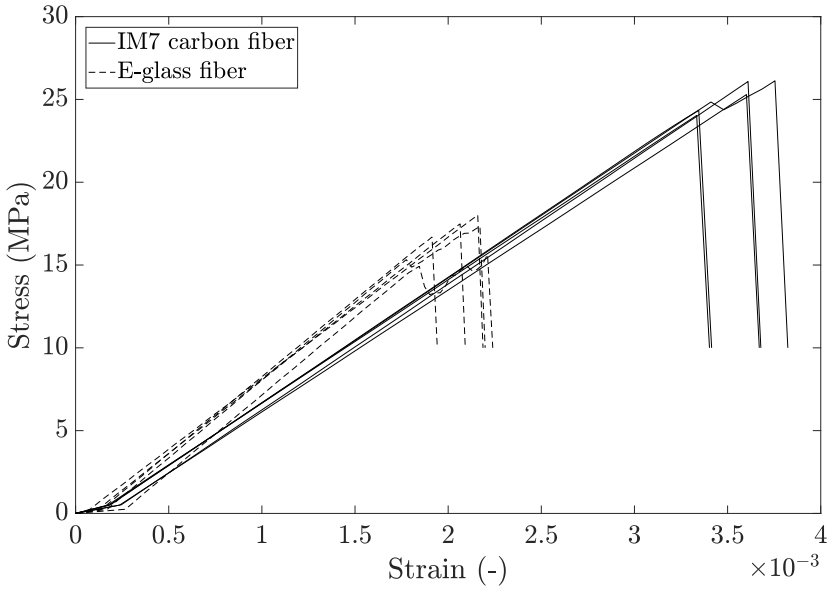

(c) Stress versus strain plots

Figure 3: Contour plots showing the end-of-cure residual stresses (maximum principal) from virtual manufacturing analysis, maximum principal stress before the onset of damage from virtual mechanical testing and damage field at the end of the virtual mechanical testing in representative (a) IM7 carbon fiber RVE ($v_f = 0.60$) and (b) E-glass fiber RVE ($v_f = 0.55$); (c) plot of stress versus strain from virtual mechanical testing of IM7 carbon and E-glass fiber RVEs.

2.3 Virtual mechanical testing

The processed RVEs at the end of the previous step were subjected to transverse tensile mechanical loads by prescribing a displacement boundary condition as illustrated in Figure 2b. The objective here was to compute the transverse composite response of the RVEs, namely the transverse tensile strength σ_{22}^{+} as a

function of their fiber volume fraction.

Failure in the matrix was modeled with a previously developed progressive damage model [32], based on the crackband theory [53]. The maximum principal stress criterion was utilized to determine failure initiation in the matrix. A traction-separation law, governed by the fracture energy, was employed to define the post-peak softening behavior of the damaging material once the critical fracture stress was reached. The critical mode I energy release rate G_{IC} was given by

$$G_{\mathrm{IC}} = h^{\eta} \int_{0}^{\bar{\epsilon}_{\mathrm{f}}^{\eta}} \bar{\sigma}_{11}^{\eta}\ \bar{\epsilon}_{11}^{\eta}\ \mathrm{d}\bar{\epsilon} \tag{6}$$

where $\bar{\sigma}_{11}^{\eta}$ and $\bar{\epsilon}_{11}^{\eta}$ are the maximum principal stress and strain values in element η, respectively; $\bar{\epsilon}_{\mathrm{f}}^{\eta}$ is the value of $\bar{\epsilon}_{11}^{\eta}$ which corresponds to a zero stress state on the post-peak stress versus strain plot; h^{η} is the characteristic length of the element η that preserves mesh objectivity by prescribing a normalized value of G_{IC} for each element, such that $g_{\mathrm{IC}}^{\eta} = G_{\mathrm{IC}}/h^{\eta}$.

A scalar damage factor D^{η} was computed to degrade the damaged element compliance components using

$$\mathrm{D}^{\eta} = 1 - \left[\frac{\sigma_{\mathrm{cr}}}{E_{\mathrm{m}}(\bar{\epsilon}_{\mathrm{f}}^{\eta} - \bar{\epsilon}_{\mathrm{init}}^{\eta})} \left(\frac{\bar{\epsilon}_{\mathrm{f}}^{\eta}}{\bar{\epsilon}_{11}^{\eta}} - 1 \right) \right] \tag{7}$$

where $\bar{\epsilon}_{\mathrm{init}}^{\eta}$ is the value of $\bar{\epsilon}_{11}^{\eta}$ when the initiation criterion ($\bar{\sigma}_{11}^{\eta} \geq \sigma_{\mathrm{cr}}$) is satisfied; E_{m} is the undamaged Young's modulus of the matrix. The damage parameter could take values between zero and one, where $D^{\eta} = 0$ meant no damage had occurred. By contrast, a maximum damage level of one corresponded to a zero-stress state on the post-peak stress versus strain plot. Also, healing was inadmissible. Once the damage factor was computed, the relevant components of the compliance matrix were degraded [32,54]. The progressive damage formulation was modeled in Abaqus/STANDARD solver with user-written subroutine UMAT. The matrix strength $\sigma_{\mathrm{cr}}^{\mathrm{m}}$ and a scaled-down fracture energy G_{IC}, corresponding to the sub-micron length scale, were prescribed to the material as listed in Table 2.

The stress versus strain plots of the five IM7 carbon fibers RVEs ($v_{\mathrm{f}} = 0.6$) and E-glass fiber RVEs ($v_{\mathrm{f}} = 0.55$), subjected to post-manufacturing transverse loads, are presented in Figure 3c. In this figure, the RVEs exhibited an initial linear-elastic response which was followed by a drop in the stress. This drop was associated with damage initiation in the matrix when the local stresses exceeded the matrix strength $\sigma_{\mathrm{cr}}^{\mathrm{m}}$. The contour plot of the maximum principal stress before the onset of damage in the representative microstructure is shown in Figure 3a for IM7 carbon and Figure 3b for E-glass fiber RVEs, respectively. Local regions with high stress concentration (corresponding to warmer colors), where failure initiation was anticipated, were clearly visible in these plots. The contour plot of the end-of-loading damage variable D, which was computed using Equation 7 and used to degrade the elements stiffness, is presented in Figures 3a and 3b, respectively for IM7 carbon and E-glass fiber RVEs. It was evident from these figures, that stress localized in regions of dense fiber packing which led to failure initiation and local microcracking. These cracks eventually coalesced

into a large crack that propagated through the microstructure resulting in a two-piece failure. The peak stress in the stress versus strain plots was regarded as the transverse composite strength σ_{22}^{+}. For the representative IM7 carbon and E-glass fiber microstructures shown in Figure 3, $\sigma_{22}^{+} = 24.03$ MPa and $\sigma_{22}^{+} = 17.49$ MPa, respectively.

The analysis was repeated for all RVEs illustrated in Figure 1 and their replicates. The transverse composite strength predictions from these analyses are summarized in Figure 4 as a function of their fiber volume fraction for IM7 carbon and E-glass fiber RVEs. Each data point in these plots was obtained by averaging the numerical predictions from five distinct replicates of an RVE of a given fiber volume fraction. The relevant standard deviations from the average values were represented by the corresponding error bars. It was clear from these figures, the fiber volume fraction manifested a strong influence on the transverse strength of the composite. The transverse composite strength predictions for IM7 carbon fiber RVEs increased steadily with the fiber volume fraction from $\sigma_{22}^{+} = 21.23 \pm 1.37$ MPa for $v_{\mathrm{f}} = 0.25$ to $\sigma_{22}^{+} = 28.65 \pm 0.71$ MPa for $v_{\mathrm{f}} = 0.75$. Similar trends were observed for E-glass fiber RVEs where the transverse strength predictions increased from $\sigma_{22}^{+} = 15.94 \pm 2.61$ MPa for $v_{\mathrm{f}} = 0.25$ to $\sigma_{22}^{+} = 20.74 \pm 0.32$ MPa for $v_{\mathrm{f}} = 0.75$. Furthermore, the fiber packing manifested a strong influence on the transverse strength. Random and densely packed fibers induce local stress concentration in composites leading to premature failure initiation and local microcracking, which typically manifests itself as large scatter of bulk composite strength. This was evident from the large standard deviations in the predicted strength values for each volume fraction in Figure 4. In particular, RVEs with lower fiber volume fraction ($v_{\mathrm{f}} = 0.25, 0.35$) manifested a relatively larger scatter associated with their predicted strength values. This suggested that the converged RVE size of 50 fibers, which was defined based on a fiber volume fraction $v_{\mathrm{f}} = 0.55$, may not be sufficiently large and representative of composite microstructures with lower fiber volume fractions. To define an appropriate RVE size for such cases, a separate statistical size effect study is warranted, which can be computationally expensive due to the larger RVE sizes that need to be analyzed. Notwithstanding that, the standard deviations for these cases were found to be within 10% of the mean values, which is within the accepted limits for numerical and physical testing. Furthermore, the predicted values were directly compared with the respective experimental strength values obtained from in-house transverse testing of thin IM7 carbon and E-glass fiber composite laminates. The predicted strength values were in excellent agreement with the experimental values as presented in Figure 4.

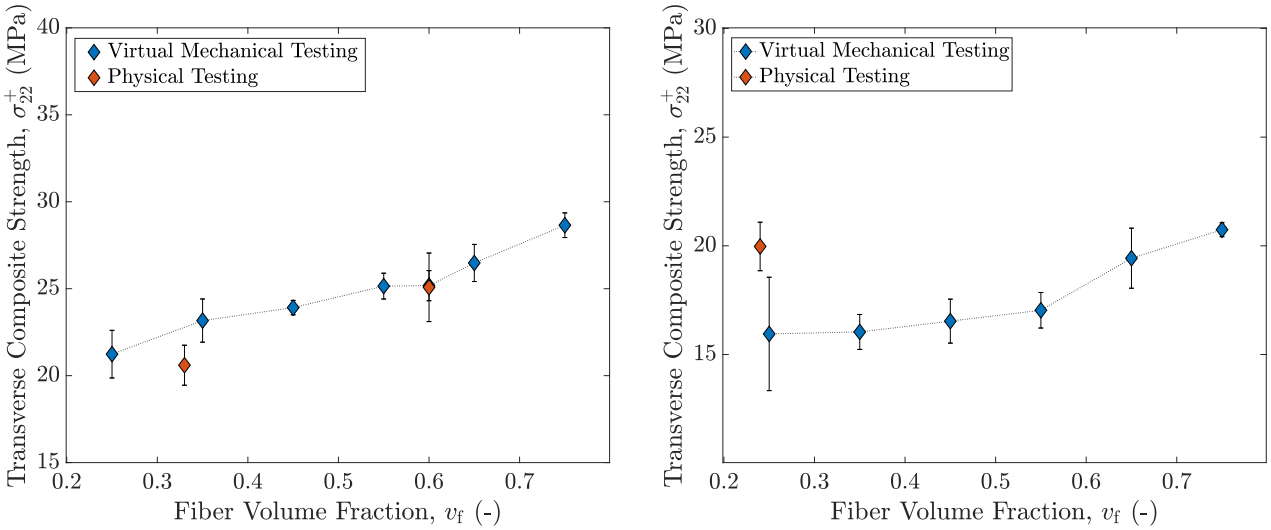

(a) IM7 carbon fiber RVEs ($d_f = 6$ μm)

(b) E-glass fiber RVEs ($d_f = 14$ μm)

Figure 4: Summary of the transverse composite strength predictions from the virtual testing of (a) IM7 carbon fiber and (b) E-glass fiber RVEs composite microstructures as a function of their fiber volume fraction.

3 Development of the Analytical Model

Modeling [21, 25, 32] and testing [55] of composites have shown that matrix failure initiates in regions of high stress concentration as a result of dense fiber packing. This concentration of stress not only depends on the constituent fiber and matrix properties but also the random fiber distribution, residual stress generation and the global fiber volume fraction that influences the transverse composite strength. This work proposed an analytical model that directly accounted for these parameters in Equation 8

$$\sigma_{22}^{+} = \sigma_{22}^{+}\left(E^{\mathrm{m}}, E_{22}^{\mathrm{f}}, \nu^{\mathrm{m}}, \nu^{\mathrm{f}}, \sigma_{\mathrm{cr}}^{\mathrm{m}}, \mathbf{SCF}_{22}^{+}\right) \tag{8}$$

specifically, the transverse composite strength σ_{22}^{+} was expressed as a function of the constituent fiber/matrix elastic properties E^{m}, E_{22}^{f}, ν^{m}, ν^{f}, the in-situ matrix strength $\sigma_{\mathrm{cr}}^{\mathrm{m}}$ and a stress concentration factor $\mathbf{SCF}_{22}^{+}$. Results from Section 2 also showed that the relative distance between the neighboring fibers and their orientation with respect to the loading direction significantly influenced stress localization between them which eventually resulted in failure initiation. Therefore, the SCF was divided into two contributions, one that accounted for the effect of the fiber distribution (distance between the fiber centers and their orientation), $\mathbf{SCF}_{\mathrm{I}}$, and the second that accounted for the effect of the fiber volume fraction, $\mathbf{SCF}_{\mathrm{II}}$. $\mathbf{SCF}_{22}^{+}$ was defined by,

$$\mathbf{SCF}_{22}^{+} = \mathbf{SCF}_{\mathrm{I}}\left(\delta, \theta\right) \times \mathbf{SCF}_{\mathrm{II}}\left(v_{\mathrm{f}}\right) \tag{9}$$

where, δ is the shortest distance between a fiber pair while θ is the orientation of that shortest distance with respect to the loading direction and v_{f} is the fiber volume fraction. The composite transverse strength can be

calculated starting from the definition of stress concentration as shown in Equation 10

$$\sigma_{22}^{+} = \frac{\sigma_{\text{cr}}^{\text{m}}}{\mathbf{SCF}_{\text{I}} \times \mathbf{SCF}_{\text{II}}} \tag{10}$$

Solving for σ_{22}^{+} required the determination of the SCFs. A novel computational approach to calculate the $\mathbf{SCF}_{\text{I}}$ and $\mathbf{SCF}_{\text{II}}$ for a multi-fiber RVE is proposed below.

3.1 Stress concentration factor

A stress concentration factor is defined as the ratio of the stresses in the proximity of a discontinuity within a continuum and the far-field/applied stress averaged over a boundary surface. In case of composite microstructures, a fiber inclusion within a matrix is a discontinuity that acted as a stress-riser. A simple linear-elastic analysis of a single IM7 carbon fiber embedded in an infinite RIM R135-H1366 medium yielded an SCF = 1.45. This meant the stresses in the vicinity of a fiber were 1.45 times higher that the applied stresses. A similar value of SCF = 1.54 was obtained for E-glass fibers embedded in the same RIM R135-H1366 epoxy matrix. While such results from a single-fiber RUC have been extensively used to develop analytical models for transverse composite strength, they fail to provide useful information about the non-uniform stress field in a multi-fiber RUC. In such cases, the neighboring fibers influence the stress distribution around the fiber being considered, which then affects the stress concentration surrounding it. This evaluation of a global SCF in a multi-fiber microstructures becomes increasingly challenging since the non-uniform stress field is not only influenced by several neighboring fiber interactions within a certain proximity δ but also their relative orientation with respect to the loading direction θ.

To determine the SCF in multi-fiber microstructures, a unique stress concentration analysis was proposed in this study. First, the influence of introducing a neighboring fiber on the local SCF was investigated with a two-fiber model (see Section 3.2). Following this, a correlation was established between the geometrical variations in a multi-fiber microstructure and the SCF by virtue of the nearest neighbor statistical descriptor (see Section 3.3).

3.2 Influence of fiber arrangement on SCF

The influence of fiber arrangement on the SCF was investigated through FE simulations. Several two-fiber models, as illustrated in Figures 5 and 6, were generated in Abaqus/STANDARD with $0^\circ \leq \theta \leq 90^\circ$ and 6.1 μm $\leq \delta \leq$ 26 μm for IM7 carbon fiber models while $0^\circ \leq \theta \leq 90^\circ$ and 14.1 μm $\leq \delta \leq$ 34 μm for E-glass fiber models, respectively. Assuming a linear elastic material response, these models were subjected to transverse mechanical loads by prescribing a displacement boundary condition. The SCF in each case was determined using the classic definition,

$$\mathbf{SCF}_{\text{I}} = \frac{\sigma_{\max}}{\sigma_{\infty}} \tag{11}$$

where, $\sigma_{\max}$ is the maximum principal point stress and σ_{∞} is the far-field/applied principal stress. The computed $\mathbf{SCF}_{\mathrm{I}}$ for various combinations of δ and θ are shown in Figures 5a and 5b for IM7 carbon fibers and Figures 6a and 6b for E-glass fibers, respectively. For a given value of $\delta = 7.2$ μm in Figure 5a, the highest stress concentration was observed when the fiber centers were oriented parallel to the loading direction ($\theta = 0°$). The $\mathbf{SCF}_{\mathrm{I}}$ rapidly decreased from 2.52 to 1.45 as θ increased from 0° to 90°. By contrast, the $\mathbf{SCF}_{\mathrm{I}}$ gradually reduced from 3.13 to 1.56 in Figure 5b as the distance between the fiber centers δ increased from 6.2 μm to 15 μm while $\theta = 0°$. A consistent trend was observed for E-glass fiber models as illustrated in Figures 6a and 6b. The influence of relative fiber arrangement on the local SCF was clearly evident from these figures. By analyzing an exhaustive combination of δ and θ, an interpolation function for $\mathbf{SCF}_{\mathrm{I}}(\delta, \theta)$ was developed (see Figures 5c and 6c),

$$\mathbf{SCF}_{\mathrm{I}}(\delta, \theta) = a_{11} + a_{12}\theta + a_{21}\delta + a_{22}\theta\delta + a_{23}\delta^2 \tag{12}$$

where, $a_{11} - a_{23}$ are fitting parameters specific to the material systems considered in this study. These values for both IM7 carbon and E-glass fiber models are summarized in Table 3. Note, these values were different for the two fiber materials analyzed in this study and that their values may further vary for other material systems. This function, defined by Equation 12 and the corresponding fitting parameters, were utilized in the subsequent section to determine the $\mathbf{SCF}_{\mathrm{I}}$ of each multi-fiber microstructure analyzed in the previous section as a function of their geometrical variations.

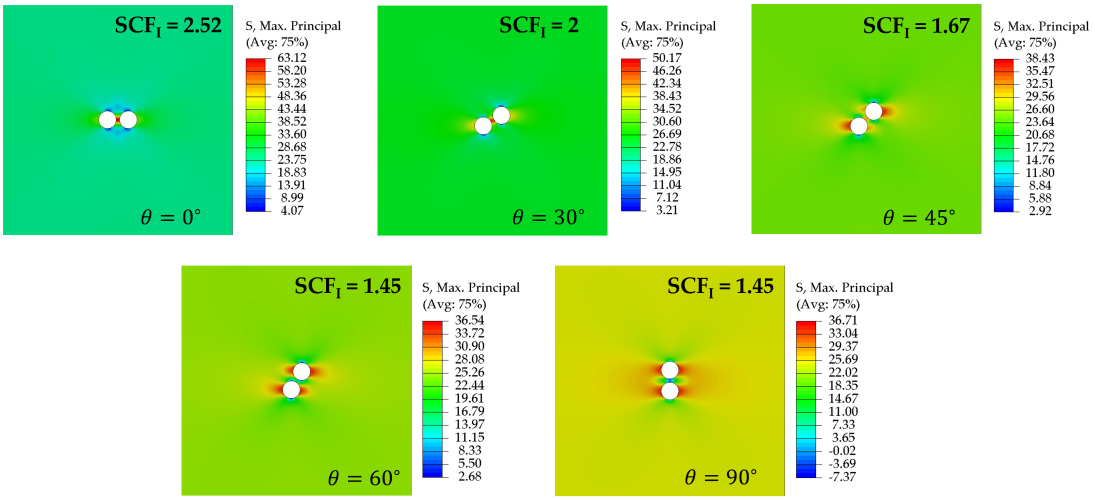

(a) Variation in $\mathbf{SCF_I}$ with θ when $\delta = 7.2$ μm

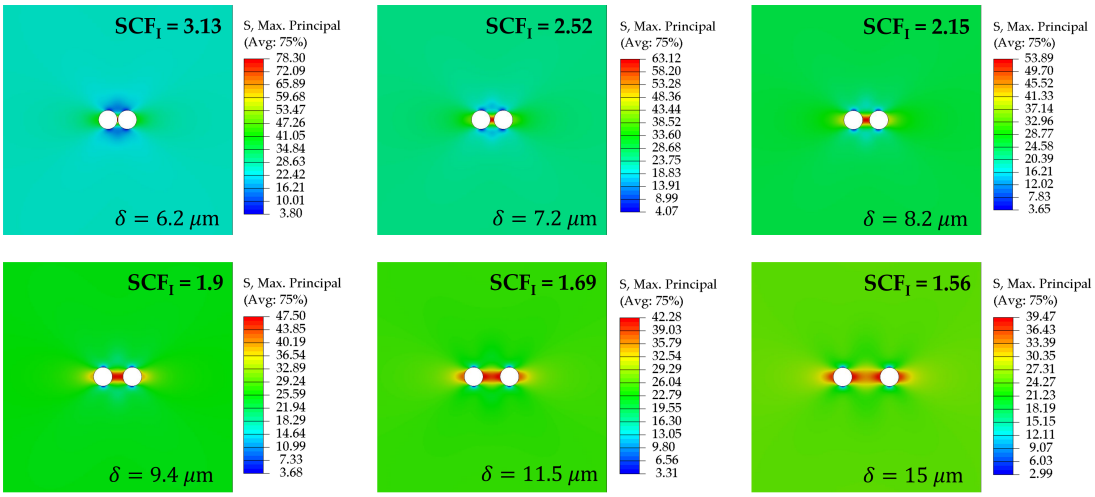

(b) Variation in $\mathbf{SCF_I}$ with δ when $\theta = 0°$

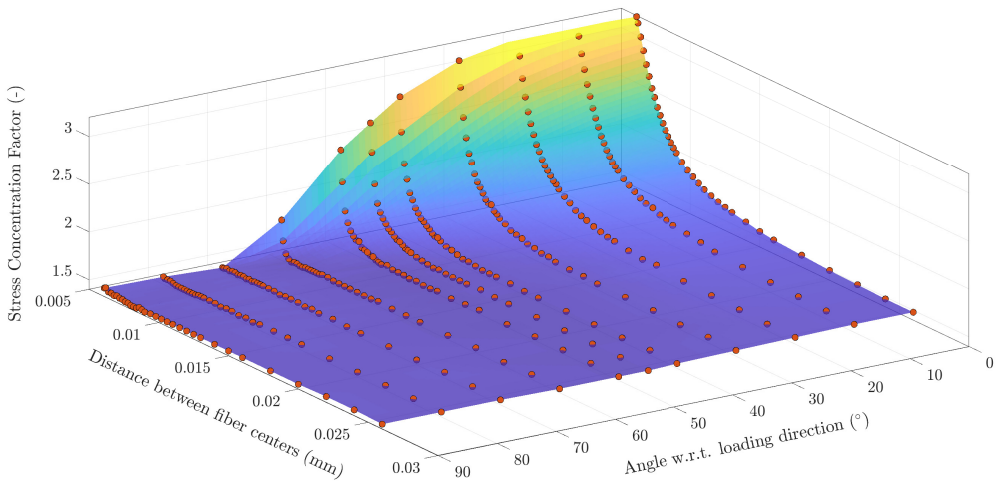

(c) Variation in $\mathbf{SCF_I}$ with θ and δ

Figure 5: Variation in $\mathbf{SCF_I}$ in IM7 carbon fiber microstructures with (a) fiber orientation θ and (b) distance between the fiber centers δ (fibers not shown); (c) interpolation function expressing $\mathbf{SCF_I}$ as a function of θ and δ.

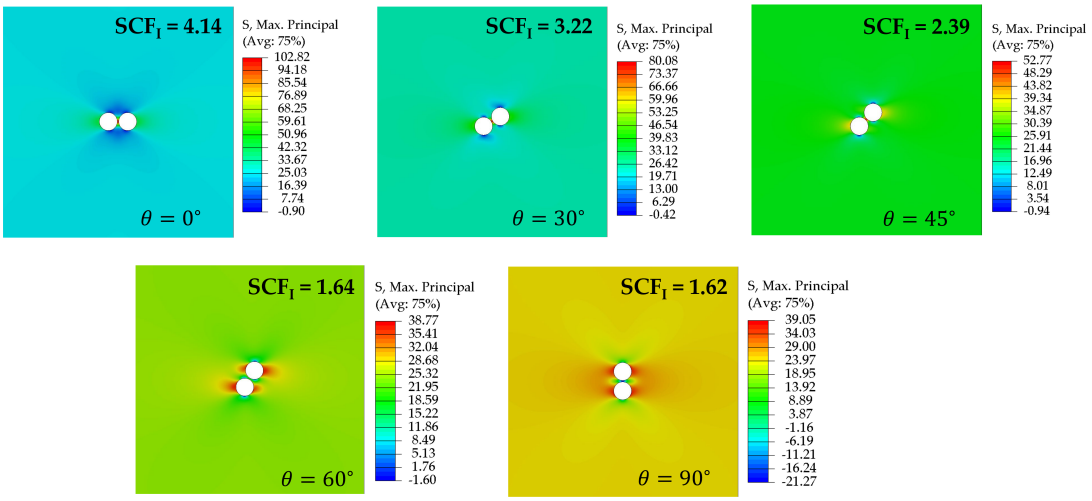

(a) Variation in $\mathbf{SCF}_\mathrm{I}$ with θ when $\delta = 15.2$ μm

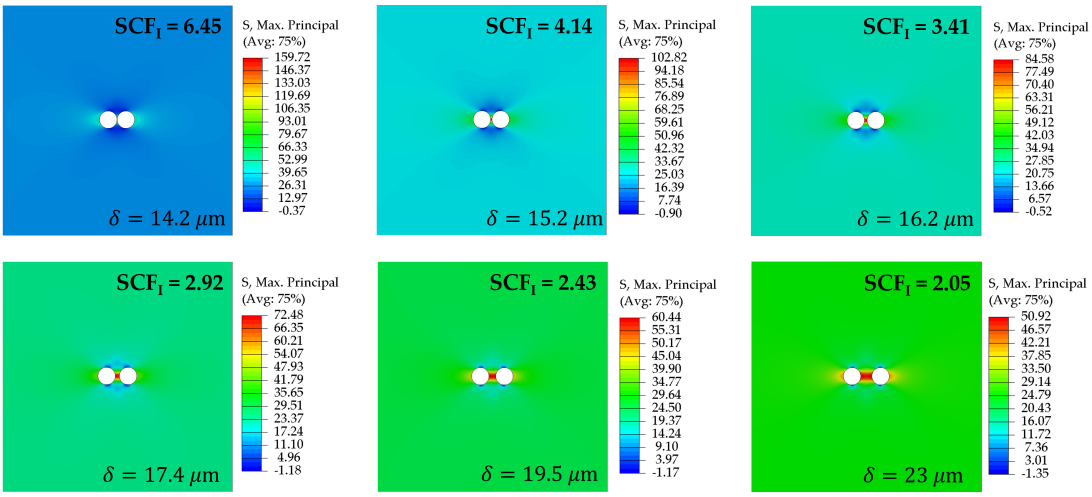

(b) Variation in $\mathbf{SCF}_\mathrm{I}$ with δ when $\theta = 0°$

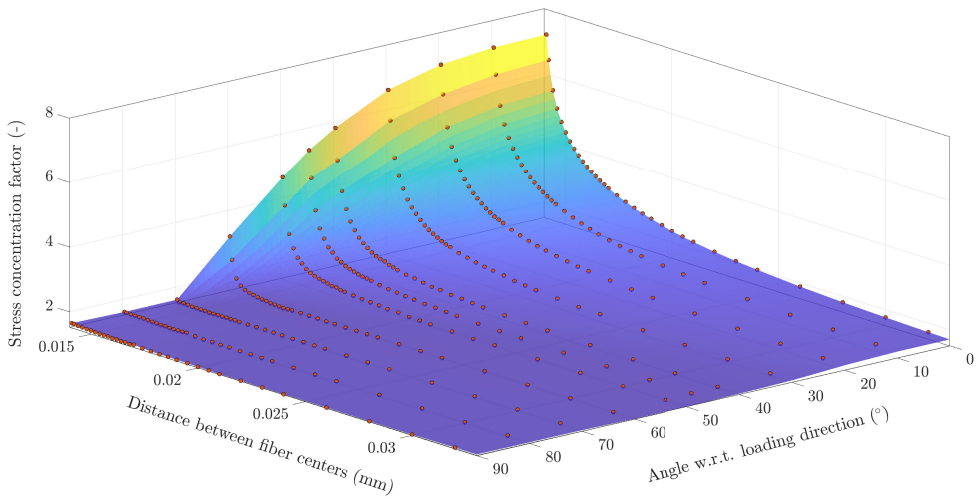

(c) Variation in $\mathbf{SCF}_\mathrm{I}$ with θ and δ

Figure 6: Variation in $\mathbf{SCF}_\mathrm{I}$ in E-glass fiber microstructures with (a) fiber orientation θ and (b) distance between the fiber centers δ (fibers not shown); (c) interpolation function expressing $\mathbf{SCF}_\mathrm{I}$ as a function of θ and δ.

Table 3: Material system-specific fitting parameters used for the analytical model predictions.

Parameter [-]		**IM7 carbon**	**E-glass**
SCF	Single fiber RUC	1.45	1.54
a_{11}		3.698	13.3
a_{12}		-1.872×10^{-2}	-7.035×10^{-2}
a_{21}	Equation 12	-2.123×10^{-1}	-7.86×10^{-1}
a_{22}		-9.742×10^{-4}	2.508×10^{-3}
a_{23}		-4.645×10^{-3}	1.278×10^{-2}
b		2.99×10^{-1}	1.336×10^{-1}
c	Equation 13	5.916	8.449
d		-5.882	-8.811

3.3 SCF in multi-fiber microstructures

Several statistical descriptors have been reported in the literature to quantify the geometrical variations within the microstructures such as local fiber volume fraction distribution using Voronoi tessellation, cluster analysis with Delaunay triangulation, second-order intensity function [26, 27, 56–62]. Since the goal of this study is to quantify the local geometrical variations in the multi-fiber microstructures analyzed in Section 2 and to establish a direct correlation with the global $\mathbf{SCF}_{\mathrm{I}}$, the nearest neighbor statistical descriptor was utilized which is based on the short-range fiber interactions. The definition of this descriptor is illustrated schematically in Figure 7. For a given fiber center i in the microstructure, the algorithm identified its closest neighbor and measured the distance between the fiber centers δ^i along with its relative orientation θ^i with respect to the loading direction. This process was repeated for all fiber centers in the microstructure. The mean shortest distance $\bar{\delta}$ and the corresponding mean orientation $\bar{\theta}$ were computed for each microstructure. The global $\mathbf{SCF}_{\mathrm{I}}$ for each of these microstructures was then computed with the help of the interpolation function $\mathbf{SCF}_{\mathrm{I}}\left(\bar{\delta}, \bar{\theta}\right)$ (see Equation 12), where the mean shortest distance $\bar{\delta}$ and orientation $\bar{\theta}$ values from the statistical analysis were used. These values for each microstructure analyzed in this study are summarized in the appendix Tables A1 and A2.

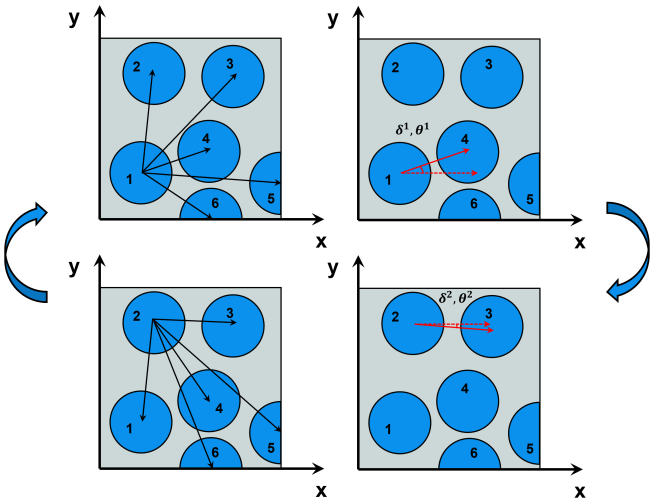

Figure 7: Schematic showing the working of the nearest neighbor distribution statistical descriptor.

By substituting into Equation 10 , the neat matrix strength $\sigma_{\text{cr}}^{\text{m}} = 64.1$ MPa (see Table 2), composite strength predictions σ_{22}^{+} of microstructures from Section 2 and the $\mathbf{SCF}_{\text{I}}$ computed using Equation 12, $\mathbf{SCF}_{\text{II}}$ was determined for each microstructure analyzed previously (see appendix Tables A1 and A2). The variation of $\mathbf{SCF}_{\text{II}}$ for each microstructure as a function of its fiber volume fraction is presented in Figure 8 for IM7 carbon and E-glass fiber models. Note that each data point on the plot is an average of five microstructure renditions with random fiber packing. A non-linear least-square regression fitting of this variation yielded an expression for $\mathbf{SCF}_{\text{II}}$,

$$\mathbf{SCF}_{\text{II}} = b + c\sqrt{v_{\text{f}}} + dv_{\text{f}} \tag{13}$$

where $b - d$ are fitting parameters specific to the material systems and microstructures considered in this study. These values for both IM7 carbon and E-glass fiber models are summarized in Table 3. Equations 12 and 13 were substituted in Equation 10 to obtain the final expression for the transverse composite strength. The analytical model, thus developed, accurately predicted the transverse strength of IM7 carbon and E-glass fiber composite microstructures for a wide range of fiber volume fractions and random fiber distributions. For instance, in Figure 9a, the model predicted close to the neat matrix strength of $\sigma_{\text{cr}}^{\text{m}} = 64.1$ MPa where $v_{\text{f}} = 0$ which is representative of neat matrix. Subsequently, a sudden drop in strength predictions was observed with the introduction of fibers due to stress concentration. This drop was followed by a steady increase in the composite strength with the fiber volume fraction. A good correlation was established between the numerical model predictions, experimental measurements and the analytical model predictions as demonstrated in Figure 9a. Consistent trends were obtained form E-glass fiber/RIM R135-H1366 microstructures as seen in Figure 9b.

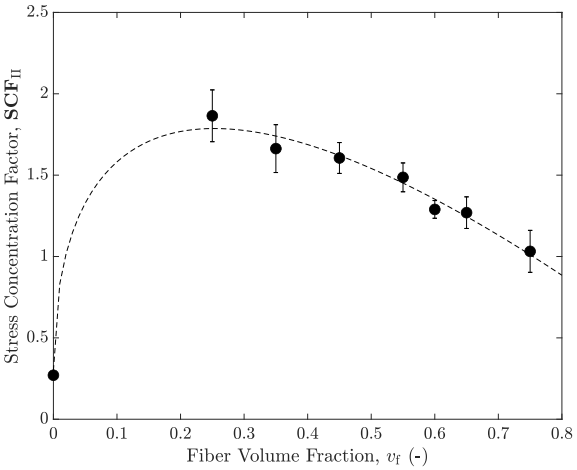

(a) IM7 carbon fiber RVEs ($d_{\mathrm{f}} = 6$ μm)

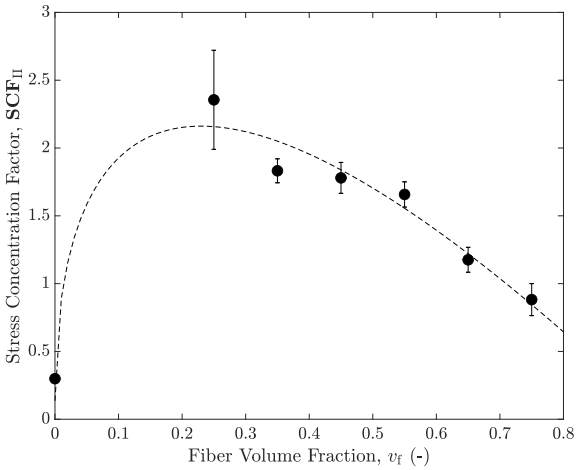

(b) E-glass fiber RVEs ($d_{\mathrm{f}} = 14$ μm)

Figure 8: Variation in $\mathbf{SCF}_{\mathrm{II}}$ with the fiber volume fraction of (a) IM7 carbon fiber and (b) E-glass fiber RVEs.

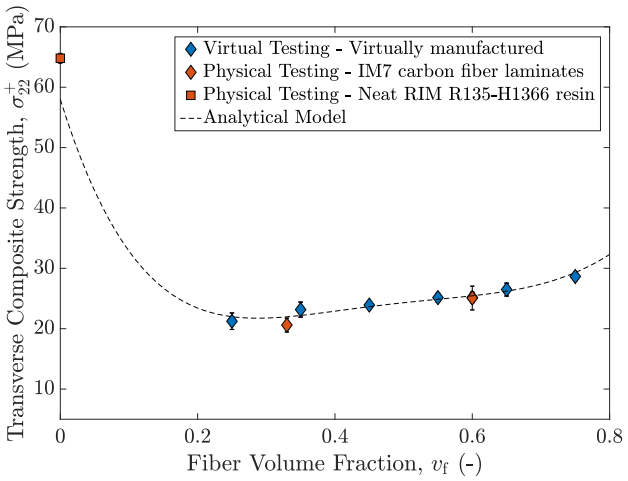

(a) IM7 carbon fiber RVEs ($d_{\mathrm{f}} = 6$ μm)

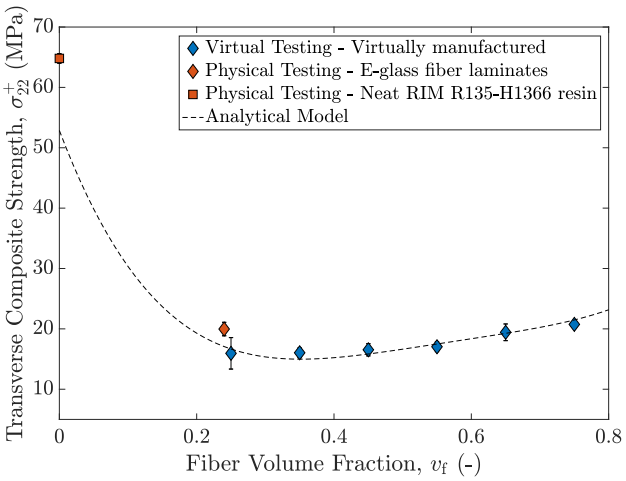

(b) E-glass fiber RVEs ($d_{\mathrm{f}} = 14$ μm)

Figure 9: Comparison of the analytical model predictions for transverse composite strength with the numerical model predictions and experimental data for (a) IM7 carbon and (b) E-glass fiber RVEs.

It should be noted that Equations 10, 12 and 13 are material system-specific and cannot be employed to predict the transverse composite response of a different constituent material system. This limitation is associated with the underlying assumption that the influence of the constituent fiber/matrix elastic properties on the SCF was implicitly accounted for in the data fitting process. As summarized in Table 3, a different set of fitting parameters were obtained for E-glass fiber microstructures. Thus, to better quantify the influence of constituent material properties on the SCF and to develop a generalized analytical mode, independent of any fitting parameters, explicit correlations between the constituent properties and the SCF must be defined. Additionally, the effect of process-induced residual stresses on the transverse strength predictions was implicitly accounted for during the data fitting process where composite strength of the virtually manufactured microstructures were used to inform the analytical model development. To explicitly determine this effect

and to account for it in the improved analytical model, further investigation into the development of residual stress and the influence of random fiber distribution is warranted. It has been shown that fiber can influence how stress is generated during processing and redistributed during subsequent loading which drives failure initiation and propagation in composites. A good understanding of these physical phenomena is necessary before its influence on the transverse composite strength can be explicitly modeled. Once its influence is quantified, a dedicated parameters can be introduced to capture the effect of process-induced residual stress on the transverse composite strength prediction. Finally, the present model was developed using the nearest neighbor distribution (based on short-range interaction) statistical descriptor to quantify the random fiber distribution and determine failure initiation in composite microstructures. However, it was observed that post-initiation, failure propagation through the microstructure not only depended on the fiber closeness near the initiation site but also on the local fiber distribution (local fiber volume fraction) that influenced residual stress generation during manufacturing and stress redistribution during subsequent mechanical loading. To quantify such geometrical variations and to fully capture their effect, more sophisticated statistical descriptors must be assessed. Despite these limitations, the proof of concept to develop a computational micromechanics-based analytical model for transverse composite strength prediction is promising and warrants further investigation.

4 Conclusions

This work presented a novel methodology to develop an analytical model for transverse composite strength for carbon and glass reinforced epoxy resin using a numerical and statistical approach. Computational micromechanical analysis, involving virtual manufacturing and testing, were carried out on composite microstructures with varying fiber volume fractions to predict their transverse composite strength. A novel stress concentration factor for multi-fiber microstructures were defined based on the nearest neighbor statistical descriptor. A material system-specific analytical model was developed for transverse strength predictions based on the computational modeling results. It was shown that computational micromechanics can provide insight on the physical mechanisms that influenced the transverse composite strength, which are otherwise extremely challenging to quantify experimentally. Accounting for such physical mechanisms, a mathematical relation was established, which linked microscale failure in composites to these physical mechanisms, to effectively predict the transverse composite strength.

Acknowledgments

This material is based upon the work supported partially by the Air Force Office of Scientific Research and the National Science Foundation under grant number IIP – 1826232. Any opinions, findings and conclusions or recommendations expressed in this material are those of the author(s) and do not necessarily reflect the views of the National Science Foundation. The authors would like to thank NASA for their support of this

research under grant numbers 80NSSC19K1246 and NNX17AJ32G.

No potential competing interest was reported by the authors.

References

[1] F. Naya, C. González, C. S. Lopes, S. Van der Veen, and F. Pons, "Computational micromechanics of the transverse and shear behavior of unidirectional fiber reinforced polymers including environmental effects," *Composites Part A: Applied Science and Manufacturing*, vol. 92, pp. 146–157, Jan. 2017.

[2] L. L. Vignoli, M. A. Savi, P. M. C. L. Pacheco, and A. L. Kalamkarov, "Micromechanical analysis of transversal strength of composite laminae," *Composite Structures*, vol. 250, p. 112546, Oct. 2020.

[3] L. L. Vignoli, M. A. Savi, P. M. C. L. Pacheco, and A. L. Kalamkarov, "Comparative analysis of micromechanical models for the elastic composite laminae," *Composites Part B: Engineering*, vol. 174, p. 106961, Oct. 2019.

[4] I. V. Andrianov, J. Awrejcewicz, and V. V. Danishevskyy, *Asymptotical Mechanics of Composites*, vol. 77 of *Advanced Structured Materials*. Cham: Springer International Publishing, 2018.

[5] A. F. Fedotov, "Mori-Tanaka experimental-analytical model for predicting engineering elastic moduli of composite materials," *Composites Part B: Engineering*, vol. 232, p. 109635, Mar. 2022.

[6] Z.-M. Huang, "On micromechanics approach to stiffness and strength of unidirectional composites:," *Journal of Reinforced Plastics and Composites*, Nov. 2018.

[7] S. Nemat-Nasser and M. Hori, *Micromechanics: Overall Properties of Heterogeneous Materials*. Elsevier, Oct. 2013.

[8] Z.-M. Huang and Y.-X. Zhou, *Strength of Fibrous Composites*. Advanced Topics in Science and Technology in China, Berlin Heidelberg: Springer-Verlag, 2012.

[9] R. M. Christensen, *Mechanics of Composite Materials*. Courier Corporation, Mar. 2012.

[10] M. W. Hyer and S. R. White, *Stress Analysis of Fiber-reinforced Composite Materials*. DEStech Publications, Inc, 2009.

[11] K. Reifsnider, G. Sendeckyj, S. Wang, W. Feng, W. Johnson, W. Stinchcomb, N. Pagano, J. Caruso, and C. Chamis, "Assessment of Simplified Composite Micromechanics Using Three-Dimensional Finite-Element Analysis," *Journal of Composites Technology and Research*, vol. 8, no. 3, p. 77, 1986.

[12] Z. Hashin, "Analysis of Properties of Fiber Composites With Anisotropic Constituents," *Journal of Applied Mechanics*, vol. 46, pp. 543–550, Sept. 1979.

[13] A. K. Mal and A. K. Chatterjee, "The Elastic Moduli of a Fiber-Reinforced Composite," *Journal of Applied Mechanics*, vol. 44, pp. 61–67, Mar. 1977.

[14] Z. Hashin and B. W. Rosen, "The Elastic Moduli of Fiber-Reinforced Materials," *Journal of Applied Mechanics*, vol. 31, pp. 223–232, June 1964.

[15] Z.-M. Huang and L.-M. Xin, "In situ strengths of matrix in a composite," *Acta Mechanica Sinica*, vol. 33, pp. 120–131, Feb. 2017.

[16] C. Chamis, "Simplified Composite Micromechanics For Predicting Microstresses," 1987.

[17] C. C. Chamis, "Simplified Composite Micromechanics Equations for Strength, Fracture Toughness, Impact Resistance and Environmental Effects.," tech. rep., NATIONAL AERONAUTICS AND SPACE ADMINISTRATION CLEVELAND OH LEWIS RESEARCH CEN TER, Jan. 1984.

[18] Z.-M. Huang, *Micromechanical Failure Analysis of Unidirectional Composites*. IntechOpen, Nov. 2018.

[19] C. C. Chamis, F. Abdi, M. Garg, L. Minnetyan, H. Baid, D. Huang, J. Housner, and F. Talagani, "Micromechanics-based progressive failure analysis prediction for WWFE-III composite coupon test cases," *Journal of Composite Materials*, vol. 47, pp. 2695–2712, Sept. 2013.

[20] S. A. Elnekhaily and R. Talreja, "Damage initiation in unidirectional fiber composites with different degrees of nonuniform fiber distribution," *Composites Science and Technology*, vol. 155, pp. 22–32, Feb. 2018.

[21] H. Ghayoor, S. V. Hoa, and C. C. Marsden, "A micromechanical study of stress concentrations in composites," *Composites Part B: Engineering*, vol. 132, pp. 115–124, Jan. 2018.

[22] T. Zhang and Y. Yan, "A comparison between random model and periodic model for fiber-reinforced composites based on a new method for generating fiber distributions," *Polymer Composites*, vol. 38, no. 1, pp. 77–86, 2017.

[23] D. Beicha, T. Kanit, Y. Brunet, A. Imad, A. E. Moumen, and Y. Khelfaoui, "Effective transverse elastic properties of unidirectional fiber reinforced composites," *Mechanics of Materials*, vol. 102, pp. 47–53, Nov. 2016.

[24] L. Bouaoune, Y. Brunet, A. El Moumen, T. Kanit, and H. Mazouz, "Random versus periodic microstructures for elasticity of fibers reinforced composites," *Composites Part B: Engineering*, vol. 103, pp. 68–73, Oct. 2016.

[25] L. Liu and Z.-M. Huang, "Stress concentration factor in matrix of a composite reinforced with transversely isotropic fibers," *Journal of Composite Materials*, vol. 48, pp. 81–98, Jan. 2014.

[26] V. Romanov, S. V. Lomov, Y. Swolfs, S. Orlova, L. Gorbatikh, and I. Verpoest, "Statistical analysis of real and simulated fibre arrangements in unidirectional composites," *Composites Science and Technology*, vol. 87, pp. 126–134, Oct. 2013.

[27] D. Trias, J. Costa, A. Turon, and J. E. Hurtado, "Determination of the critical size of a statistical representative volume element (SRVE) for carbon reinforced polymers," *Acta Materialia*, vol. 54, pp. 3471–3484, Aug. 2006.

[28] X. Liu and W. Yu, "Multiscale Modeling of Viscoelastic Behaviors of Textile Composites Using Mechanics of Structure Genome," in *2018 AIAA/ASCE/AHS/ASC Structures, Structural Dynamics, and Materials Conference*, (Kissimmee, Florida), American Institute of Aeronautics and Astronautics, Jan. 2018.

[29] X. Liu, D. Furrer, J. Kosters, and H. Holmes, "Vision 2040: A Roadmap for Integrated, Multiscale Modeling and Simulation of Materials and Systems," tech. rep., NASA, Mar. 2018.

[30] J. LLorca, C. González, J. M. Molina-Aldareguía, J. Segurado, R. Seltzer, F. Sket, M. Rodríguez, S. Sádaba, R. Muñoz, and L. P. Canal, "Multiscale Modeling of Composite Materials: a Roadmap Towards Virtual Testing," *Advanced Materials*, vol. 23, no. 44, pp. 5130–5147, 2011.

[31] S. P. Shah, S. U. Patil, C. J. Hansen, G. M. Odegard, and M. Maiarù, "Process modeling and characterization of thermoset composites for residual stress prediction," *Mechanics of Advanced Materials and Structures*, pp. 1–12, Dec. 2021.

[32] S. P. Shah and M. Maiarù, "Effect of Manufacturing on the Transverse Response of Polymer Matrix Composites," *Polymers*, vol. 13, p. 2491, Jan. 2021. Number: 15 Publisher: Multidisciplinary Digital Publishing Institute.

[33] S. U. Patil, S. P. Shah, M. Olaya, P. P. Deshpande, M. Maiaru, and G. M. Odegard, "Reactive Molecular Dynamics Simulation of Epoxy for the Full Cross-Linking Process," *ACS Applied Polymer Materials*, Oct. 2021.

[34] P. S. Gaikwad, A. S. Krieg, P. P. Deshpande, S. U. Patil, J. A. King, M. Maiaru, and G. M. Odegard, "Understanding the Origin of the Low Cure Shrinkage of Polybenzoxazine Resin by Computational Simulation," *ACS Applied Polymer Materials*, vol. 3, pp. 6407–6415, Dec. 2021. Publisher: American Chemical Society.

[35] R. J. D'Mello, A. M. Waas, M. Maiaru, and R. Koon, "Integrated Computational Modeling for Efficient Material and Process Design for Composite Aerospace Structures," in *AIAA Scitech 2020 Forum*, American Institute of Aeronautics and Astronautics. _eprint: https://arc.aiaa.org/doi/pdf/10.2514/6.2020-0655.

[36] S. Patil, S. Shah, P. Deshpande, M. Olaya, K. Kashmari, G. M. Odegard, and M. Maiaru, "Multiscale Approach to Predict Cure-Induced Residual Stresses in an Epoxy System," in *Proceedings of the American Society of Composites 35th Technical (Virtual) Conference*, American Society of Composites, Sept. 2020.

[37] S. Shah, S. Patil, P. Deshpande, A. Krieg, K. Kashmari, H. Al Mahmud, J. King, G. M. Odegard, and M. Maiaru, "Multiscale Modeling for Virtual Manufacturing of Thermoset Composites," in *AIAA Scitech 2020 Forum*, AIAA SciTech Forum, American Institute of Aeronautics and Astronautics, Jan. 2020.

[38] S. Shah and M. Maiaru, "Microscale Analysis of Virtually Cured Polymer Matrix Composites Accounting for Uncertainty in Matrix Properties During Manufacturing," in *American Society for Composites 2018*, DEStech Publications, Inc., Nov. 2018.

[39] P. P. Deshpande, S. Shah, S. Patil, K. Kashmari, M. Olaya, G. M. Odegard, and M. Maiarã™, "Multiscale Modelling of the Cure Process in Thermoset Polymers Using ICME," in *Proceedings of the American Society for Composites " Thirty-fifth Technical Conference*, vol. 0, 2020. Number: 0.

[40] M. Maiarù, R. J. D'Mello, and A. M. Waas, "Characterization of intralaminar strengths of virtually cured polymer matrix composites," *Composites Part B: Engineering*, vol. 149, pp. 285–295, Sept. 2018.

[41] M. Maiaru, "Effect of uncertainty in matrix fracture properties on the transverse strength of fiber reinforced polymer matrix composites," in *2018 AIAA/ASCE/AHS/ASC Structures, Structural Dynamics, and Materials Conference*, American Institute of Aeronautics and Astronautics, 2018.

[42] R. J. D'Mello, M. Maiarù, and A. M. Waas, "Virtual manufacturing of composite aerostructures," *The Aeronautical Journal*, vol. 120, pp. 61–81, Jan. 2016.

[43] R. J. D'Mello, M. Maiarù, and A. M. Waas, "Effect of the curing process on the transverse tensile strength of fiber-reinforced polymer matrix lamina using micromechanics computations," *Integrating Materials and Manufacturing Innovation*, vol. 4, pp. 119–136, Dec. 2015.

[44] T. S. Mesogitis, A. A. Skordos, and A. C. Long, "Uncertainty in the manufacturing of fibrous thermosetting composites: A review," *Composites Part A: Applied Science and Manufacturing*, vol. 57, pp. 67–75, Feb. 2014.

[45] F. Danzi, D. Fanteria, E. Panettieri, and M. C. Mancino, "A numerical micro-mechanical study on damage induced by the curing process in carbon/epoxy unidirectional material," *Composite Structures*, vol. 210, pp. 755–766, Feb. 2019.

[46] X. Hui, Y. Xu, J. Wang, and W. Zhang, "Microscale viscoplastic analysis of unidirectional CFRP composites under the influence of curing process," *Composite Structures*, vol. 266, p. 113786, June 2021.

[47] X. Hui, Y. Xu, and W. Zhang, "An integrated modeling of the curing process and transverse tensile damage of unidirectional CFRP composites," *Composite Structures*, vol. 263, p. 113681, May 2021.

[48] C. He, J. Ge, D. Qi, J. Gao, Y. Chen, J. Liang, and D. Fang, "A multiscale elasto-plastic damage model for the nonlinear behavior of 3D braided composites," *Composites Science and Technology*, vol. 171, pp. 21–33, Feb. 2019.

[49] L. Yang, Y. Yan, J. Ma, and B. Liu, "Effects of inter-fiber spacing and thermal residual stress on transverse failure of fiber-reinforced polymer–matrix composites," *Computational Materials Science*, vol. 68, pp. 255–262, Feb. 2013.

[50] L. G. Zhao, N. A. Warrior, and A. C. Long, "A micromechanical study of residual stress and its effect on transverse failure in polymer–matrix composites," *International Journal of Solids and Structures*, vol. 43, pp. 5449–5467, Sept. 2006.

[51] S. E. Stapleton, L. Appel, J. W. Simon, and S. Reese, "Representative volume element for parallel fiber bundles: Model and size convergence," *Composites Part A: Applied Science and Manufacturing*, vol. 87, pp. 170–185, Aug. 2016.

[52] M. R. Kamal and S. Sourour, "Kinetics and thermal characterization of thermoset cure," *Polymer Engineering & Science*, vol. 13, no. 1, pp. 59–64, 1973.

[53] Z. P. Bažant and B. H. Oh, "Crack band theory for fracture of concrete," *Matériaux et Construction*, vol. 16, pp. 155–177, May 1983.

[54] E. J. Pineda, B. A. Bednarcyk, A. M. Waas, and S. M. Arnold, "Progressive failure of a unidirectional fiber-reinforced composite using the method of cells: Discretization objective computational results," *International Journal of Solids and Structures*, vol. 50, pp. 1203–1216, May 2013.

[55] M. Flores, A. Sharits, R. Wheeler, N. Sesar, and D. Mollenhauer, "Experimental analysis of polymer matrix composite microstructures under transverse compression loading," *Composites Part A: Applied Science and Manufacturing*, vol. 156, p. 106859, May 2022.

[56] M. J. Schey, T. Beke, L. Appel, S. Zabler, S. P. Shah, J. Hu, F. Liu, M. Maiaru, and S. Stapleton, "Identification and Quantification of 3D Fiber Clusters in Fiber-Reinforced Composite Materials," *JOM*, May 2021.

[57] S. Shah, E. Plaka, M. Schey, J. Hu, F. Liu, T. Beke, S. E. Stapleton, and M. Maiaru, "In-Situ Characterization of Polymer Matrix Composites and Progressive Damage Analysis of Virtually Reconstructed Microstructures," in *Proceedings of the American Society for Composites — Thirty-fifth Technical Conference*, vol. 0, Sept. 2020.

[58] L. Maragoni, P. A. Carraro, and M. Quaresimin, "Development, validation and analysis of an efficient micro-scale representative volume element for unidirectional composites," *Composites Part A: Applied Science and Manufacturing*, vol. 110, pp. 268–283, July 2018.

[59] S. H. R. Sanei, E. J. Barsotti, D. Leonhardt, and R. S. Fertig, "Characterization, synthetic generation, and statistical equivalence of composite microstructures," *Journal of Composite Materials*, vol. 51, pp. 1817–1829, June 2017.

[60] L. Yang, Y. Yan, Z. Ran, and Y. Liu, "A new method for generating random fibre distributions for fibre reinforced composites," *Composites Science and Technology*, vol. 76, pp. 14–20, Mar. 2013.

[61] T. J. Vaughan and C. T. McCarthy, "A combined experimental–numerical approach for generating statistically equivalent fibre distributions for high strength laminated composite materials," *Composites Science and Technology*, vol. 70, pp. 291–297, Feb. 2010.

[62] A. R. Melro, P. P. Camanho, and S. T. Pinho, "Generation of random distribution of fibres in long-fibre reinforced composites," *Composites Science and Technology*, vol. 68, pp. 2092–2102, July 2008.

A Analysis Summary

Table A1: Analysis summary for IM7 carbon fiber RVEs.

RVE ID	$\boldsymbol{v_f}$ (-)	σ_{22}^{+} (MPa)	δ (mm)	θ (°)	$\mathbf{SCF_I}$ (-)	$\mathbf{SCF_{II}}$ (-)
CF-25-1	0.25	18.68	8.194 ± 1.46	41 ± 32	1.61	2.14
CF-25-2	0.25	22.48	8.214 ± 1.82	39 ± 30	1.64	1.74
CF-25-3	0.25	21.27	7.835 ± 1.53	47 ± 27	1.55	1.94
CF-25-4	0.25	22.36	7.563 ± 1.24	40 ± 26	1.69	1.69
CF-25-5	0.25	21.39	7.835 ± 1.61	40 ± 25	1.66	1.81
CF-35-1	0.35	24.36	7.34 ± 1.2	41 ± 28	1.72	1.53
CF-35-2	0.35	22.97	7.213 ± 0.92	47 ± 24	1.63	1.71
CF-35-3	0.35	21.93	7.078 ± 0.91	47 ± 24	1.63	1.79
CF-35-4	0.35	24.82	7.219 ± 0.85	40 ± 26	1.77	1.46
CF-35-5	0.35	21.75	7.479 ± 1.34	46 ± 28	1.61	1.84
CF-45-1	0.45	23.38	6.997 ± 0.86	51 ± 26	1.58	1.74
CF-45-2	0.45	24.66	6.71 ± 0.41	52 ± 24	1.62	1.60
CF-45-3	0.45	23.79	6.749 ± 0.44	51 ± 24	1.63	1.65
CF-45-4	0.45	23.91	6.942 ± 0.81	46 ± 27	1.69	1.59
CF-45-5	0.45	23.82	6.751 ± 0.39	42 ± 24	1.86	1.45
CF-55-1	0.55	25.96	6.582 ± 0.25	46 ± 27	1.81	1.37
CF-55-2	0.55	24.51	6.606 ± 0.34	50 ± 27	1.70	1.54
CF-55-3	0.55	25.59	6.559 ± 0.28	50 ± 23	1.73	1.44
CF-55-4	0.55	24.03	6.592 ± 0.32	52 ± 27	1.64	1.63
CF-55-5	0.55	25.66	6.572 ± 0.32	50 ± 23	1.71	1.46
CF-60-1	0.6	26.08	6.512 ± 0.26	43 ± 26	2.01	1.22
CF-60-2	0.6	26.12	6.478 ± 0.19	48 ± 26	1.81	1.36
CF-60-3	0.6	24.34	6.465 ± 0.19	45 ± 27	1.95	1.35
CF-60-4	0.6	24.03	6.501 ± 0.28	40 ± 24	2.09	1.28
CF-60-5	0.6	25.29	6.532 ± 0.3	41 ± 25	2.04	1.24
CF-65-1	0.65	26.85	6.457 ± 0.17	42 ± 25	2.09	1.14
CF-65-2	0.65	27.82	6.403 ± 0.09	46 ± 29	1.98	1.16
CF-65-3	0.65	24.60	6.436 ± 0.24	46 ± 28	1.96	1.33
CF-65-4	0.65	26.24	6.396 ± 0.15	49 ± 27	1.85	1.32
CF-65-5	0.65	26.89	6.428 ± 0.15	52 ± 25	1.72	1.39
CF-75-1	0.75	29.54	6.309 ± 0.01	44 ± 25	2.21	0.98
CF-75-2	0.75	27.65	6.301 ± 0.01	39 ± 30	2.39	0.97
CF-75-3	0.75	28.09	6.302 ± 0.01	40 ± 23	2.33	0.98
CF-75-4	0.75	28.68	6.315 ± 0.03	54 ± 19	1.74	1.29
CF-75-5	0.75	29.29	6.302 ± 0.01	40 ± 24	2.33	0.94

Table A2: Analysis summary for E-glass fiber RVEs.

RVE ID	$\boldsymbol{v_f}$ (-)	σ_{22}^{+} (MPa)	δ (mm)	θ (°)	$\mathbf{SCF_I}$ (-)	$\mathbf{SCF_{II}}$ (-)
EGF-25-1	0.25	18.51	18.945 ± 4.01	50 ± 26	1.62	2.14
EGF-25-2	0.25	18.44	18.051 ± 4.11	51 ± 28	1.65	2.11
EGF-25-3	0.25	11.78	18.037 ± 4.3	45 ± 23	1.77	3.08
EGF-25-4	0.25	14.19	17.664 ± 3.83	39 ± 25	1.97	2.29
EGF-25-5	0.25	16.82	17.522 ± 3.44	47 ± 25	1.77	2.16
EGF-35-1	0.35	14.89	16.473 ± 1.94	45 ± 30	2.19	1.97
EGF-35-2	0.35	15.80	16.36 ± 2.64	45 ± 26	2.30	1.76
EGF-35-3	0.35	16.53	16.68 ± 2.72	51 ± 26	2.25	1.72
EGF-35-4	0.35	17.27	16.717 ± 2.1	48 ± 25	2.04	1.82
EGF-35-5	0.35	15.70	16.321 ± 1.7	40 ± 24	2.16	1.89
EGF-45-1	0.45	18.33	15.395 ± 1.46	46 ± 27	2.19	1.60
EGF-45-2	0.45	16.11	15.566 ± 1.95	43 ± 28	2.30	1.73
EGF-45-3	0.45	16.02	15.911 ± 1.61	41 ± 25	2.25	1.78
EGF-45-4	0.45	16.85	15.835 ± 2.3	46 ± 28	2.04	1.87
EGF-45-5	0.45	15.37	15.786 ± 2.47	44 ± 22	2.16	1.93
EGF-55-1	0.55	17.34	15.229 ± 1.21	49 ± 28	2.09	1.77
EGF-55-2	0.55	18.02	15.177 ± 0.92	46 ± 25	2.34	1.52
EGF-55-3	0.55	15.64	15.117 ± 0.84	42 ± 24	2.59	1.58
EGF-55-4	0.55	17.49	15.178 ± 0.85	49 ± 23	2.12	1.73
EGF-55-5	0.55	16.69	15.172 ± 1.04	47 ± 26	2.28	1.69
EGF-65-1	0.65	18.57	14.65 ± 0.44	43 ± 27	3.09	1.12
EGF-65-2	0.65	18.69	14.803 ± 0.52	47 ± 26	2.59	1.33
EGF-65-3	0.65	20.31	14.674 ± 0.44	45 ± 27	2.93	1.08
EGF-65-4	0.65	21.69	14.775 ± 0.39	47 ± 26	2.64	1.12
EGF-65-5	0.65	17.89	14.763 ± 0.6	43 ± 25	2.90	1.24
EGF-75-1	0.75	20.75	14.39 ± 0.17	43 ± 24	3.74	0.83
EGF-75-2	0.75	21.32	14.439 ± 0.3	36 ± 23	4.08	0.74
EGF-75-3	0.75	20.37	14.397 ± 0.11	46 ± 25	3.40	0.92
EGF-75-4	0.75	20.69	14.38 ± 0.15	52 ± 21	2.85	1.09
EGF-75-5	0.75	20.57	14.454 ± 0.21	41 ± 26	3.71	0.84